



Microstructural Features and Functional Assessment of the Kidney Using Diffusion MRI

18

Suraj D. Serai, Sila Kurugol, Pim Pullens, Zhen Jane Wang, and Eric Sigmund

DWI in the Kidney: Background

Diffusion is a physical process that results from the thermally driven, random motion of water molecules. Diffusion-weighted imaging (DWI) provides an image contrast that is dependent on the molecular motion of water (diffusion), which is called Brownian motion. After Stejskal and Tanner [1] described a DW SE T2-weighted pulse sequence in NMR spectroscopy with two extra gradient pulses equal in magnitude and opposite in phase accumulation (Fig. 18.1), it took several decades for that sequence to become clinically feasible [2] due to limitations of MR

equipment and imaging trajectories. In pure water, molecules undergo free, thermally agitated diffusion (with a three-dimensional Gaussian distribution). The width of the Gaussian distribution expands with the elapsed time, and the average square of this width per unit time gives the units of the apparent diffusion coefficient (ADC). In tissues, the term “apparent diffusion” is utilized since the movement of water molecules is modified by their interactions with cell membranes, macromolecules, and flow processes. Through measurement of this apparent diffusion, diffusion MRI provides insight into the microscopic details of tissue architecture and microcirculation.

DWI provides an image contrast using a “diffusion weighted” spin echo T2-weighted pulse sequence with two extra gradient pulses equal in magnitude and opposite in phase accumulation. This is done by modifying a standard T2-weighted imaging sequence by applying a symmetric pair of diffusion sensitizing gradients on either side of the 180° refocusing pulse. Moving water protons acquire a phase shift from the first diffusion-sensitizing gradient, which, as a consequence of motion, is not entirely rephased by the second gradient, resulting in attenuation of the measured signal intensity. Hence, the presence of water diffusion is observed as signal loss on diffusion-weighted MR images. However, it took several decades for that sequence to become clinically feasible [2] due to limitations of MR equipment, especially the gradient hard-

S. D. Serai (✉)
Children’s Hospital of Philadelphia, University of Pennsylvania, Philadelphia, PA, USA
e-mail: serais@chop.edu

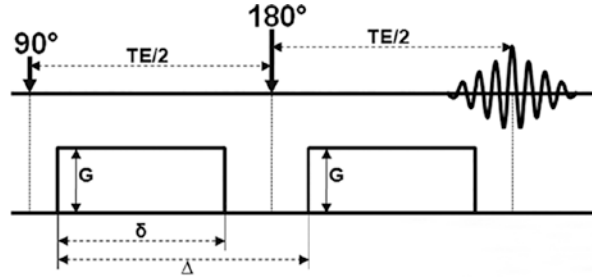
S. Kurugol
Harvard Medical School, Boston, MA, USA
e-mail: Sila.Kurugol@childrens.harvard.edu

P. Pullens
University of Antwerp, Antwerp University Hospital, Edegem, Belgium
e-mail: Pim.Pullens@uzgent.be

Z. J. Wang
University of California San Francisco, San Francisco, CA, USA
e-mail: Zhen.Wang@ucsf.edu

E. Sigmund
NYU Langone Health, New York, NY, USA
e-mail: Eric.Sigmund@nyulangone.org

Fig. 18.1 Timing diagram of Stejskal–Tanner based diffusion acquisition sequence



ware. With recent advances in gradient hardware technology, high field scanners, RF coil design improvements, and image reconstruction innovations, DW MR imaging is reaching a potential for clinical use in the abdomen, particularly in the kidney. DW MR imaging is an attractive technique for multiple reasons: it can potentially add useful qualitative and quantitative information to conventional imaging sequences; it is rapid (performed within a breath-hold or can be performed free breathing with respiratory gating) and can be easily incorporated to existing clinical protocols.

Diffusion Measurements and ADC

In the most common and first approximation to the magnetization behavior with diffusion-weighting in tissue, the signal intensity (SI) of a diffusion-weighted image is best expressed as

$$\frac{S}{S_0} = \exp(-b \cdot ADC) \quad (1.1)$$

where S_0 is the signal intensity on a T2-weighted ($b = 0$) image, and b is the diffusion weighting factor, which is directly proportional to the square of the gyromagnetic ratio, the square of the magnitude of the gradient pulses, and three powers of

gradient duration. The degree of diffusion weighting applied to an image is expressed by its b -value. The b -values are limited by the gradient hardware, but values of several hundreds to thousands are easily achievable on clinical MRI scanners (Fig. 18.2).

Diffusion is often not isotropic (same in all directions) in biological tissues since water diffuses more easily along the direction of globally aligned microstructural elements (such parallel tubules in renal medulla) rather than across them (diffusion anisotropy) [3, 4]. Because cellular structures are distributed anisotropically, the measurement of diffusion is also direction-dependent [4], emphasizing the need for measuring diffusion in several directions (Fig. 18.3). Thus, to obtain a rotationally invariant estimate of isotropic diffusion, diffusion-weighted images must be acquired in at least three orthogonal directions. The postprocessing of these images begins with the calculation of the natural logarithms of the images, which should be averaged to form a rotationally invariant (or “trace-weighted”) resultant image. Using a linear least-squares regression on a pixel-by-pixel basis, the resultant image and the natural logarithm of the reference T2-weighted image are fitted to the b -values to calculate ADC, which is the negative slope of the fitted line.

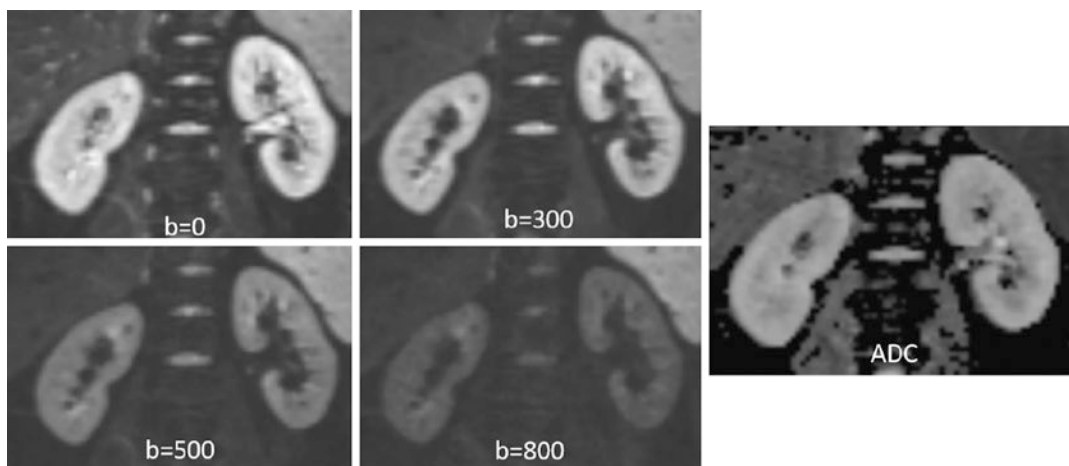


Fig. 18.2 Representative images of kidneys with increasing b -values and corresponding ADC map



Fig. 18.3 Schematic representation of directionality. Rate of diffusion depends on the direction

IVIM (Microcirculation/ Microstructure)

Given the prominent role that both perfusion and tubular flow play in the filtration process, one of the key extensions of the single compartment ADC representation for renal tissue is the inclusion of microcirculatory motion in addition to hindered Brownian motion. The most common approach to do so is the intravoxel incoherent motion (IVIM) model, one of the first signal descriptions in the history of DWI that has in the prior decade experienced a renaissance of use as technology has permitted its application to highly perfused organs [5–8]. The biophysical model of IVIM is a two-compartment description: molecular diffusion in tissues and microcirculatory motion in vessels/tubules. This approximation describes flow of blood through capillaries as a diffusion process (albeit a much faster one), due to the often-distributed orientations of flow within a capillary network. To separate the effects of diffusion and perfusion on the DW signal, a biexponential model is employed:

$$\frac{S}{S_0} = f \exp(-bD^*) + (1-f) \exp(-bD) \quad (18.2)$$

where f is the flowing blood fraction, D^* is the pseudo diffusion coefficient associated with blood microcirculation, and D the apparent diffusivity in the tissue space. In most cases, the pseudo diffusion coefficient associated with blood microcirculation is much larger (about ten times larger) than the water diffusion coefficient in tissues. The basic interpretation of the IVIM parameters are that (a) D reflects microstructure of the extravascular parenchymal space from restricted/hindered diffusion, (b) f represents flow volume, and (c) D^* reflects a combination of blood velocity and microcirculatory architecture.

The IVIM signature was observed in preclinical renal MRI as early as 1991 [9], and many subsequent studies explored its contrast in human kidney MRI. In particular, literature reviews [10–12] have indicated that much of the reported variability in renal ADC values can be traced to the use of variable b -values across studies. Since the

single compartment ADC description does not capture the full IVIM signal behavior, measurements from different b -value combinations admit differing amounts of perfusion effects into the ADC parameter, which confounds study comparison. For this reason, among others, consensus statements have encouraged standardized b -value choices for studies that are to be pooled or compared to other trials.

As summarized in recent reviews [12, 13], IVIM metrics have been extensively reported in healthy and pathologic kidney tissue. Key findings include correlation of diffusion metrics (often D^* and f) with glomerular filtration rate (GFR), in some cases more strongly than that of ADC. Several disease processes (allograft dysfunction, acute pyelonephritis, polycystic disease, obstruction, renal artery stenosis, and chronic kidney disease) have been investigated with IVIM in smaller-scale studies, with trends of useful biomarkers from the IVIM model emerging. Conversely, diversity of acquisition/analysis parameters prevents large-scale conclusions given the current evidence, again supporting standardization efforts in the future.

DTI (Anisotropy)

Another microstructural feature beyond the ADC description is that of anisotropy. Due to the common orientation of microstructural barriers to transport in some tissue types such as renal medulla, the rate of apparent diffusion depends on direction, with largest diffusion occurring parallel to, and lowest diffusion perpendicular to, oriented structures such as renal tubules in medullary pyramids. The measurement and analysis framework that captures this behavior, as applied initially to the brain and later to many other organs (spine, muscle, breast, and kidney) is termed diffusion tensor imaging (DTI). DTI is based on the application of diffusion gradients in different directions in space, enabling the evaluation of the movement of water molecules in 3D and whether there is a dominant direction to diffusion restriction, which allows to determine

fiber tracts according to the dominant direction of water movement in each voxel. DTI generalizes the ADC approach by incorporating images acquired with diffusion gradients in multiple directions to determine the directionality (i.e., anisotropy) of apparent diffusion. DTI metrics help provide rotationally invariant indices that describe the properties of the diffusion profile. DTI provides several quantitative parameters including fractional anisotropy (FA) and apparent diffusion coefficient (ADC) and also allows to generate primary eigenvector maps (Fig. 18.4). The amount of diffusion is characterized by ADC, and the anisotropy of diffusion is characterized by FA. FA is a normalized, dimensionless index that measures the properties of anisotropy of DTI. Mathematically, at least six noncollinear directions are required given the need to calculate six independent elements of the symmetric 3×3 diffusion tensor D_{ij} [14], an anisotropic but still Gaussian description of water motion. The tensor is then diagonalized to its principal frame

$$D_{ij} = \begin{pmatrix} \lambda_1 & 0 & 0 \\ 0 & \lambda_2 & 0 \\ 0 & 0 & \lambda_3 \end{pmatrix} \quad (18.3)$$

where its diagonal elements (eigenvalues) are the principal diffusivities, their average is the mean diffusivity (MD), and their corresponding eigenvectors (v_1 , v_2 , and v_3) define the principal diffusion directions [15]. The direction that corresponds to the largest eigenvalue (usually chosen to be λ_1) is called the axial or parallel direction, while the other two directions are called the radial or perpendicular directions. The axial diffusivity is given by

$$D_{\parallel} \equiv \lambda_1, \quad (18.4)$$

and the radial diffusivity is given by

$$D_{\perp} \equiv \frac{1}{2}(\lambda_2 + \lambda_3) \quad (18.5)$$

Anisotropy indices are different combinations of the directional diffusion coefficients, such as the normalized variance called fractional anisotropy (FA),

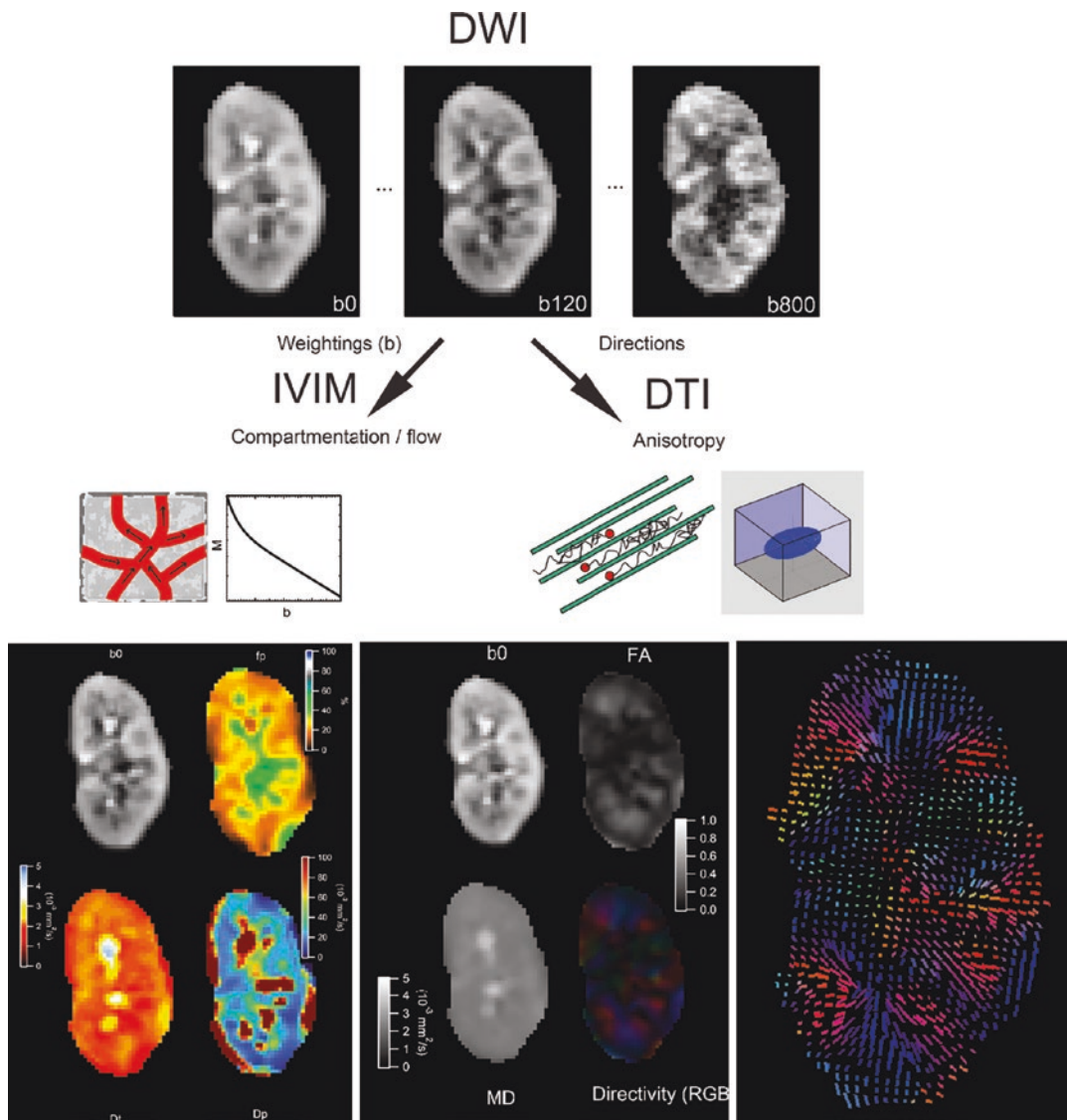


Fig. 18.4 Example intravoxel incoherent motion (IVIM) and diffusion tensor imaging (DTI) maps from a healthy volunteer left kidney. Left: biexponential IVIM fitting of multiple b -value data provides maps of perfusion fraction

(f_p), tissue diffusion (D_t), and pseudo diffusivity (D_p). Right: DTI tensor fitting of multidirectional data provides maps of mean diffusivity (MD), fractional anisotropy (FA), directivity, and principal diffusion orientation (v_1)

$$FA = \sqrt{\frac{3 \sum_{i=1}^3 (\lambda_i - MD)^2}{2 \sum_{i=1}^3 \lambda_i^2}} \quad (18.6)$$

The FA varies from 0 to 1 and quantifies the degree to which a tissue is anisotropic. FA reflects how dominant one particular water movement direction in a voxel is and is measured from 0 to

1; while ADC measures the directionally averaged diffusivity. Low FA values imply similar diffusion along all directions, while higher FA implies that there is a marked directional dependence such that diffusion occurs preferentially along one dominant direction.

In other organs such as the brain or skeletal muscle, optimization studies have been conducted to determine b -value and number of direc-

tions choices to minimize noise-induced bias or uncertainty [16, 17]; a minimum of 20 or 30 directions are typically recommended, but it is advised to apply diffusion-weighted images in many directions as allowed by scan time limitation [17, 18].

The “radial” pattern of tubule/duct orientation in the renal medulla is well known in diffusion tensor imaging [19–23] following an initial demonstration by Ries et al. [24]. In addition to depiction of this pattern in discrete images, another application of DTI is tractography, which generates continuous streamlines as virtual representation of the anisotropic structures influencing apparent diffusion.

While only a few examples have been published [20, 22], they clearly illustrate the radial path from medullary pyramids through renal pelvis and ureter.

A wide range of studies have probed DTI methods in both healthy and diseased kidney [25, 26]. Quantitatively, common findings are that glomerular filtration rate (GFR) correlates significantly with both mean diffusion MD and fractional anisotropy FA, consistent with their partial sensitivity to the vascular/tubular flow that affects filtration. Pathologic tissue often shows decreases in MD and FA, and often a decrease in corticomedullary differentiation in these parameters (Figs. 18.5 and 18.6).

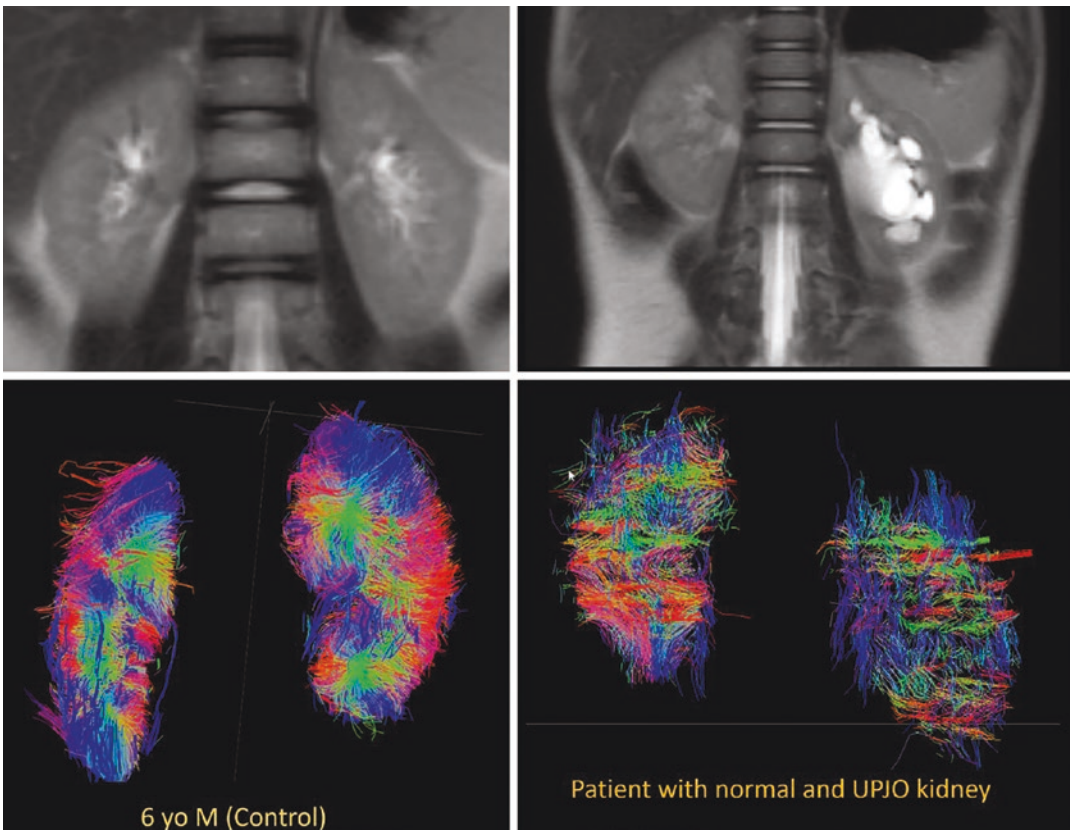


Fig. 18.5 DTI-based tractography shows microstructural disarrangement in kidneys with ureteropelvic junction obstruction [25]

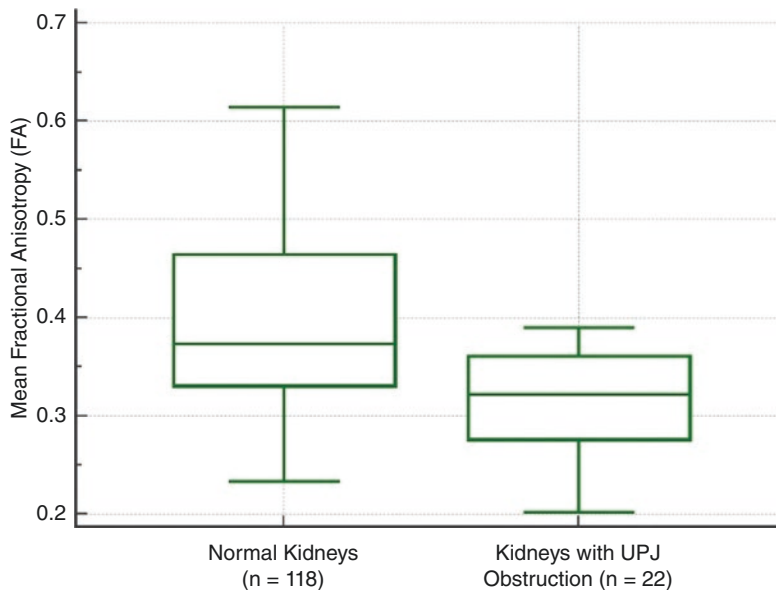


Fig. 18.6 Box and whisker plot of mean FA in normal kidneys vs patients with ureteropelvic junction (UPJ) obstruction. Horizontal lines within boxes represent medians, and vertical lines and whiskers represent the lowest and highest observations within 1.5 interquartile ranges of

lower and upper quartiles, respectively. Mean FA values were significantly lower (0.31 ± 0.07 ; $n = 22$) in kidneys with UPJ obstruction than normal kidneys (0.40 ± 0.08 ; $n = 118$) [25]

Advanced/Hybrid Models

While signatures of microcirculation and anisotropy are now unmistakable in renal DWI, their interpretation, biologic validation, and modification by disease remain topics of research. In particular, multiple circulatory networks coexist in renal cortex and medulla (glomeruli, vasa recta, proximal/distal tubules, loops of Henle, and collecting ducts) and disentangling their individual contributions to the DWI signal is nontrivial. A variety of advanced approaches have been pursued to do so, either combining existing methods (IVIM and DTI) or varying acquisition parameters (echo time, diffusion time, cardiac phase, and gradient waveform).

Flow Anisotropy

Intuitively, microscopic flow contributes to medullary anisotropy just as microstructure does, as indirectly suggested by DTI studies showing ele-

vated anisotropy when lower b -values were employed [23]. Directly, several studies have now shown that the flow term shows a similar orientation pattern. One experimental demonstration employed multiple b -value, multiple direction data to illustrate this collinear anisotropy of structural, and pseudo diffusion in a combined IVIM/DTI scheme [27], showing a pseudo diffusion anisotropy comparable to that of microstructure. This approach also yielded diagnostic potential in the assessment of renal function in pre-surgical renal mass patients [28]. One of the measures most sensitive to asymmetric laterality in kidney diffusion—reflecting the compensatory redistribution of flow in response to a neoplasm—was axial medullary pseudo diffusion. Another approach employed an intravoxel oriented flow (IVOF) model incorporating an apparent flow fraction tensor to capture the microcirculation and microstructural anisotropy in medullary tissue [29]. Another study employed a separate tensorial description for all three IVIM parameters (D, f, D^*) and showed high fractional anisotropy

for all three in the medullary compartment [30]. These studies have confirmed that the best representation of water transport in kidney should incorporate directionality in both flow and structural degrees of freedom.

Encoding Variations

As with other organs, diffusion contrast varies with various MRI encoding or acquisition parameters, in a way that may be exploited to improve the biophysical interpretation of the approach. Not surprisingly, given the strong role of perfusion in renal DWI, the cardiac phase has been shown to be a powerful modulator of renal DWI metrics in cardiac-gated imaging studies. These have included ADC [31, 32], IVIM [33, 34], and DTI [35] studies that show pseudo diffusion, perfusion fraction, and anisotropy all maximizing in systolic phase compared to diastolic phase.

Diffusion time, or the duration allotted for water spins to explore the microenvironment, is another variable that affects diffusion contrast. Microstructural barriers reduce water diffusion below the thermodynamic free diffusion value, such that apparent diffusion tends to decrease with increasing diffusion time. If the timescale associated with dominant hindrance scales l ($t \sim l^2/2D$) approximates accessible diffusion times, this provides a means of contrast modulation and potential biophysical modeling. Conversely, microcirculatory flow that gives rise to pseudo diffusion effects can also induce a diffusion time dependence as spins advance through the network. This trend is typically opposite to the microstructural one as pseudo diffusion increases in a short-time ballistic limit and finally saturates in a long-time pseudo diffusive limit. While very little systematic variation of diffusion time has been performed for renal DWI, recent work [36] employing both spin echo and stimulated echo DTI measurements suggests that in the diffusion time range of 20–125 ms, microcirculation effects predominate and apparent diffusion and anisotropy increase with diffusion time. This observation, which could be further explored

with quantitative modeling or increased sampling, is another example of the key importance of microcirculation in renal tissue water transport.

Finally, as discussed above, the known physiology of renal tissue clearly indicates that the conventional IVIM representation of one microcirculatory and one parenchymal compartment is only a first-order approximation to the reality. Multiple sources of microcirculation, both vascular (arteries, veins, capillaries, glomeruli, and vasa recta) and tubular (proximal/distal convoluted tubule, loops of Henle, and collecting ducts), contribute to pseudo diffusion, and separating their influences might dramatically improve specificity. One approach to doing so is via rate of pseudo diffusion, and several studies have shown that three compartments [37] or more generally a spectrum of diffusion coefficients [38, 39] are more descriptive of renal tissue than the conventional IVIM model. In these studies, the fastest component is typically assigned to vascular volume, while the intermediate rate compartment is interpreted as tubular flow.

Another effect on DWI contrast is through gradient waveform, which can be chosen to modulate the degree of sensitivity to steady flow (i.e., flow encoding or compensation). Specifically, constant velocity motion induces a phase shift proportional to the first moment of the gradient waveform (M_1), and in the presence of heterogeneous flow, these phase shifts interfere and induce IVIM contrast. Gradient waveforms, by varying or nulling M_1 (flow compensated, $M_1 = 0$), can correspondingly vary this attenuation, which can aid IVIM signal analysis and biophysical modeling. Flow compensated IVIM measurements have been shown in phantom [40–42], brain [43–45], liver [46–48], placenta [49], and heart [50] studies; in one study of the liver, a continuous range of gradient moments M_1 was implemented for more complete contrast variation and tissue modeling [46]. In the case of renal tissue, only pilot studies have been performed [47, 51] that modulate M_1 , and their analysis regarding multiple flow compartments is still in development. However, this variable may prove promising in disentangling renal flow compartments.

Both evidence generation and modeling in the space of advanced kidney DWI continue to evolve, as does their interpretation. However, it seems likely the conventional IVIM description will eventually give way to a more nuanced treatment for maximum biological specificity.

Advanced Readouts (SMS, RS-EPI, rFOV, Non-Cartesian)

The most common readout for kidney DWI is single shot echo-planar imaging (ss-EPI), in which all required lines of k-space are acquired in a single echo train, typically in a Cartesian pattern. The EPI technique is used to achieve very fast image acquisition in order to minimize the effects of subject motion and to retain high SNR [52, 53]. As EPI is a 2D imaging technique, volumes are acquired slice-by-slice with repetition times (TR) being set sufficiently long to both minimize T1 contrast and accommodate the whole volume of interest. Due to the length of the echo train in comparison with the transverse relaxation time $T2^*$, however, ss-DWI suffers blurring, distortion, and ghosting, which limit spatial resolution and reduce image quality. Image post-processing can ameliorate these issues to some extent, such as EPI image dewarping via reversed phase encoding acquisition as has been shown in several kidney DWI studies [54–56]. Beyond correcting EPI, however, a variety of alternatives has therefore been deployed throughout the body, some of which have been applied to kidney imaging. Some are based on single-shot turbo spin echo (TSE) acquisitions, to avoid the gradient echo-based sensitivities of EPI [57, 58]. Multiband approaches such as simultaneous multi-slice (SMS) acquisition have been used to accelerate the slice dimension [59–65], as in other organs [66–68]. Reduced field of view (rFOV) DWI captures a smaller subvolume to limit EPI echo train length and associated artifacts, providing high resolution DWI in the kidney [58, 69–71].

Multi-shot DWI EPI techniques offer higher spatial resolution but are susceptible to motion-

induced phase errors since each individual shot may have suffered different slight coherent motions from pulsation, respiration, etc. Without correction, this results in ghosting artifacts, pixel misregistration, and low image resolution with poor diffusion contrast in the reconstructed images [72], resulting in inaccurate measurements. Readout-segmented EPI (rs-EPI) alters the conventional EPI trajectory by acquiring all phase encodes but restricting the readout acquisition in each shot as a means of limiting susceptibility artifacts [73, 74]. Each of these methods, either as modifications or alternatives of standard EPI-DWI, broadens the available toolbox of kidney DWI and provides hope for higher spatial resolution, which is often crucial for proper quantification when corticomedullary differentiation deteriorates with reduced renal function. However, the variability in execution, parameter choice, and interpretation limits their broad utility now such that concerted efforts for broad translation of one alternative or another would be a valuable next step.

Diffusion Data Acquisition Methods

Acquisition method standardization is an important milestone in the validation of DWI-based parameters as imaging biomarkers for renal disease. The international collaboration on renal imaging (PARENCHIMA) has proposed technical recommendations on three variants of renal DWI, mono-exponential DWI, IVIM, and DTI, as well as associated MRI biomarkers (ADC, D , D^* , f , FA, and MD) to aid ongoing international efforts on methodological harmonization. In their recommendations, reported DWI biomarkers from 194 prior renal DWI studies were extracted and Pearson correlations between diffusion biomarkers and protocol parameters were computed. Based on the literature review, surveys were designed for the consensus building. Survey data were collected via Delphi consensus process on renal DWI preparation, acquisition, analysis, and reporting (Table 18.1). Consensus was defined as $\geq 75\%$ agreement. Summary of the literature and

Table 18.1 Imaging protocol recommendations for image acquisition of renal diffusion dataset

Protocol option	Recommendation		
Patient preparation	Normal hydration status		
Field strength	1.5 T or 3 T		
Sequence	Single shot EPI		
Orientation	Oblique coronal		
Matrix size	>128		
In-plane resolution	2–3 mm		
Slice thickness	>4 mm		
Coverage	Full kidney		
Parallel imaging factor	2		
Fat suppression	SPAIR		
TR (s)	4		
TE (msec)	Minimum (<100)		
No. of averages	3		
Breathing mode	Respiratory gated		
Cardiac gating	Not required		
Diffusion gradients	Monopolar		
	ADC	IVIM	DTI
No. of b -values	4 or 5	>6	2 or more
Suggested b -values	0, 100, 200, 400, 800	0, 30, 70, 100, 200, 400, 800	0, 400, 800
No. of directions	3	3	12 or more
Distortion correction	Yes		
Image registration	Yes		
Diffusion units	$10^{-3} \text{ mm}^2/\text{s}$		

survey data as well as recommendations for the preparation, acquisition, processing, and reporting of renal DWI were then provided in a published manuscript [12]. Diffusion tensor properties among field strength 1.5 T and 3 T were also highlighted (Fig. 18.7).

The following sections contain guides for carrying out each of these protocols on clinical scanners; these guides are stated in general terms as precise implementations may vary amid different vendor solutions.

DW-EPI for ADC

Sequence: Select a spin echo-based sequence with echo-planar imaging (EPI) readout with a diffusion preparation module. While single refocused monopolar is suggested for consensus, twice-refocused spin echo (TRSE) with bipolar gradients is acceptable.

b -values: The diffusion weighting factors b and gradient sensitizing directions are then adjusted.

Choose your b -values to the following values: 0, 100, 200, 400, 800 s/mm^2 over three orthogonal directions; this is often labeled as Trace-weighted or three-scan trace encoding.

Repetition time (TR): choose at least 4 s for sufficient signal-to-noise per time (SNR/t) efficiency. TR will be limited by the length of the excitation pulse, length of echo train, and the number of slices you acquire.

Echo time (TE): use the shortest TE allowable given all b -values selected.

Acquisition bandwidth (BW): This should be chosen as a balance between short inter-echo spacing and therefore minimum echo time on the one hand, and sufficient signal-to-noise ratio on the other. If the bandwidth is too slow, long readout duration will lead to T2-weighted signal loss; if it is too high, then high frequency noise can overwhelm the primary signal. For clinical renal MRI, a typical compromise is $\sim 2 \text{ kHz}/\text{pixel}$.

Fat saturation: Choose a method of fat saturation, using chemical shift contrast, T1 contrast, or both. The recommended approach is spectral adiabatic inversion recovery (SPAIR) to combine both chemical shift and T1 contrast for fat suppression.

Respiratory gating: This is essential to reduce motion artifacts, motion blurring, and unwanted intensities variations among the images acquired with different b -values. If this is not available, consider retrospective motion correction with dedicated software (see section below).

Geometry: Choose as phase-encoding direction the L-R direction and adapt the geometry so

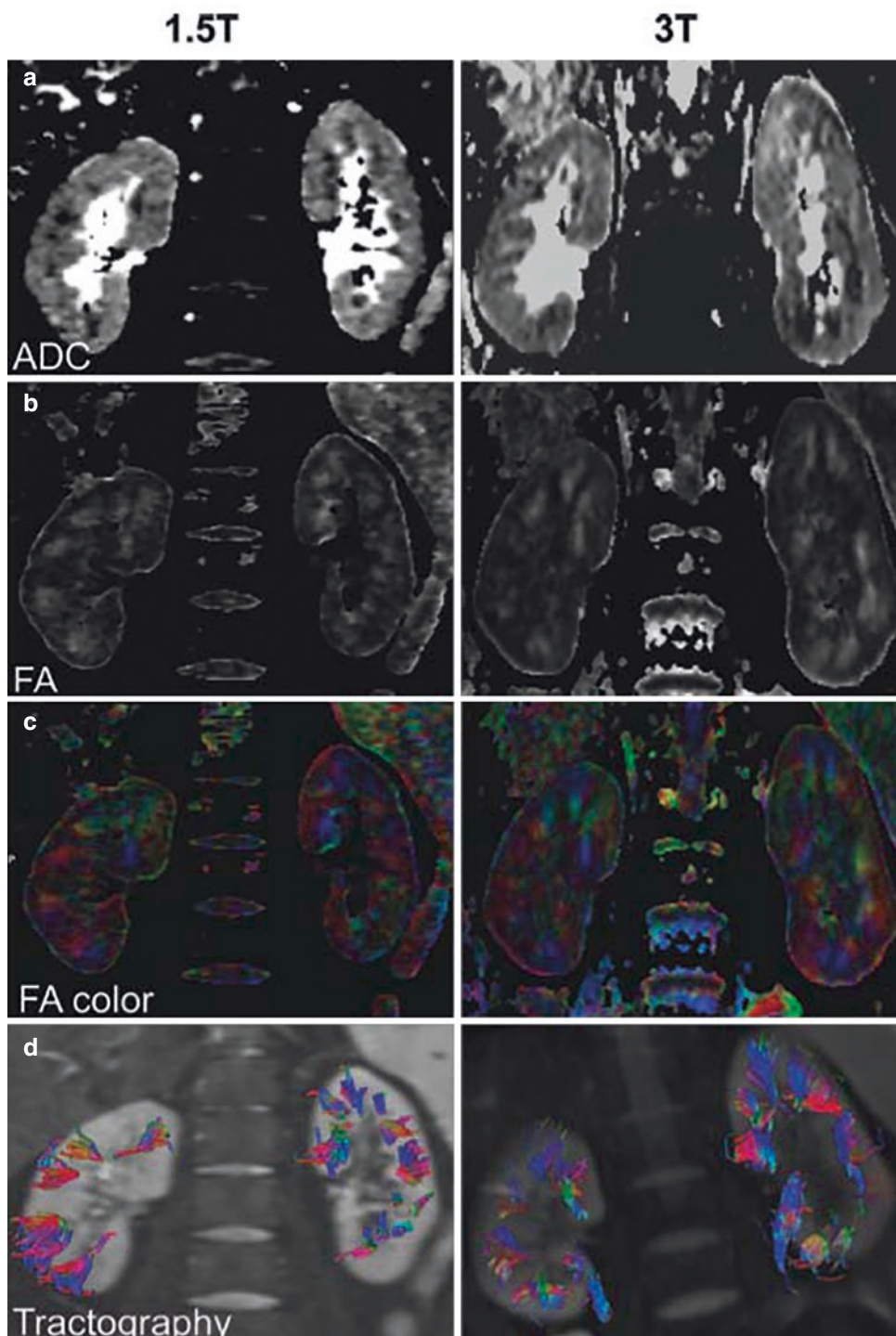


Fig. 18.7 Diffusion properties at 1.5 T and 3 T do not show significant differences. (a) ADC maps: ADC of the cortex is significantly higher than ADC of the medulla both at 1.5 T and 3 T. (b) FA maps: FA of the medulla is significantly higher than of the cortex both at 1.5 T and 3 T. In FA maps, the renal pelvis appears smaller, because cortex and pelvis both exhibit an almost isotropic diffu-

sion, so that discrimination between both compartments is hampered. (c) The color-coded FA maps allows identification of the diffusion direction (red: left-right; blue: head-foot; green: anterior-posterior). (d) Tractography reveals a typically radial diffusion direction in the medulla reflecting the radial organization of anatomic structures like vessels and tubules [75]

that the FOV in this direction includes the entire region. Use frequency encoding in head-feet (rostral-caudal) direction to avoid severe aliasing.

Averages: Increase the number of averages to improve signal-to-noise ratio by a factor of $\sqrt{\text{averages}}$, especially important for higher b -values (use three averages as a recommendation).

DW-EPI for IVIM

Load the DW-EPI sequence with the same parameters as DWI-EPI for ADC (TE, TR, matrix size, averages, and bandwidth). Increase the number of b -values to at least 6 (e.g., 0, 30, 70, 100, 200, 400, 800 s/mm^2) to probe fast diffusion from microcirculation.

DW-EPI for DTI

For DTI acquisitions, employ the same imaging parameters as suggested for ADC imaging above, use several b -values (suggested 0, 400, 800 s/mm^2), and select multiple gradient directions for each b -value. At least six noncollinear directions are required for DTI analysis, with more typically acquired for improved tensor estimation (recommended at least 12 for kidney DTI).

Motion Management

Kidney DW-MRI is sensitive to physiological motion (respiratory, peristaltic, and pulsatile). For instance, when using multi-shot acquisitions where different portions of k -space are obtained following separate signal excitations, severe artifacts may appear, due to the presence of inconsistent motion-related phase offsets across shots [76]. Therefore, kidney DW-MRI acquisition is typically performed with rapid single shot echo planar imaging sequences. With this type of acquisition, each image is acquired very fast, minimizing the effect of motion within a slice. However, rapid pulsatile motion may still lead to

artifacts and signal void in the image [77]. Also, during the acquisition of the entire set of DW-MR images, respiratory motion causes displacement of the kidneys and misalignment of slices acquired at the same position across different repetitions and diffusion encodings. This misalignment reduces the accuracy and robustness of quantitative parameter maps obtained from DW-MR images. Also, image quality degrades due to blurring because of motion, when averaging multiple repetitions of misaligned images to increase signal-to-noise ratio.

To minimize the effects of motion, DW-MR images are commonly either acquired during a breath-hold period, at the expense of the signal-to-noise ratio and spatial coverage, which may not even be feasible for some patients, or using respiratory triggering methods at the expense of increased scan time and remaining effect of motion in triggered acquisitions [78]. Respiratory triggering can be performed either using a respiratory belt type sensor wrapped around the abdomen or with an image navigator located at the diaphragm [79]. The triggering technique does not always perform well if the respiratory rhythm is irregular as in the case of anxious awake children who are breathing rapidly or irregularly. Residual motion artifacts may remain in respiratory triggered scans, and triggered scans have low efficiency as no data is acquired in most parts of the breathing cycle.

Another alternative approach used to compensate for respiratory motion is to either retrospectively perform triggering by accepting data from a certain phase of the breathing cycle and discarding the rest or sort each repetition into discrete motion states over the breathing cycle [80] based on the trajectory of periodic respiratory motion from the navigator signal. However, inaccuracies of the navigator signal can hinder correct sorting of the data into motion states. Also, volumes for certain motion states can have missing slices due to lower sampling rate per motion state. Irregular respiratory rhythm or rapid breathing can exacerbate these problems.

Another approach is non-rigid image registration of individual images for alignment. A simple approach is using non-rigid registration of a sin-

gle image slice in 2D to the corresponding slice in the reference volume. A normalized mutual information metric may be used to register images acquired with different diffusion encodings and therefore have different contrast. However, single slice registration methods cannot correct for the motion between slices.

A more accurate approach is using a rigid 3D slice-to-volume image registration separately for each kidney. This approach uses the image features of 2D slices, each acquired in about 200 ms [81]. This rapid acquisition of each slice allows effective estimation of physiological motion via a slice-to-volume image registration algorithm [55], which was first developed for the brain [82]. A 3D motion-free reference volume is registered to each 2D slice including the region of interest for each kidney using a rigid transform (Fig. 18.8). The approach is most effective in coronal acquisitions where the motion is happening mostly in plane, and a motion-free reference volume is selected among one of the acquired

$b = 0$ volumes. However, slice to volume registration is an ill-posed problem. Therefore, the rigid motion parameters can be tracked and regularized based on the information content of the sequentially acquired DW-MRI slices, using a robust state estimation with Kalman filtering instead of predicting the motion parameters for each slice independently [81]. The estimated motion parameters are then applied to correct the position of each slice in 3D. As a result of applying the estimated transformation to each 2D slice for motion correction, a scattered 3D point cloud is obtained for each 3D volume. It is possible to resample these scattered points to a regular 3D grid to reconstruct a motion-corrected 3D volume. Alternatively, a quantitative model such as IVIM or DTI can be fitted using a 3D neighborhood of points around each grid point using a kernel function for weighting each point based on their distance to the grid center and using least squares fitting to estimate the model parameters. The rigid 3D SVR will correct for the rigid

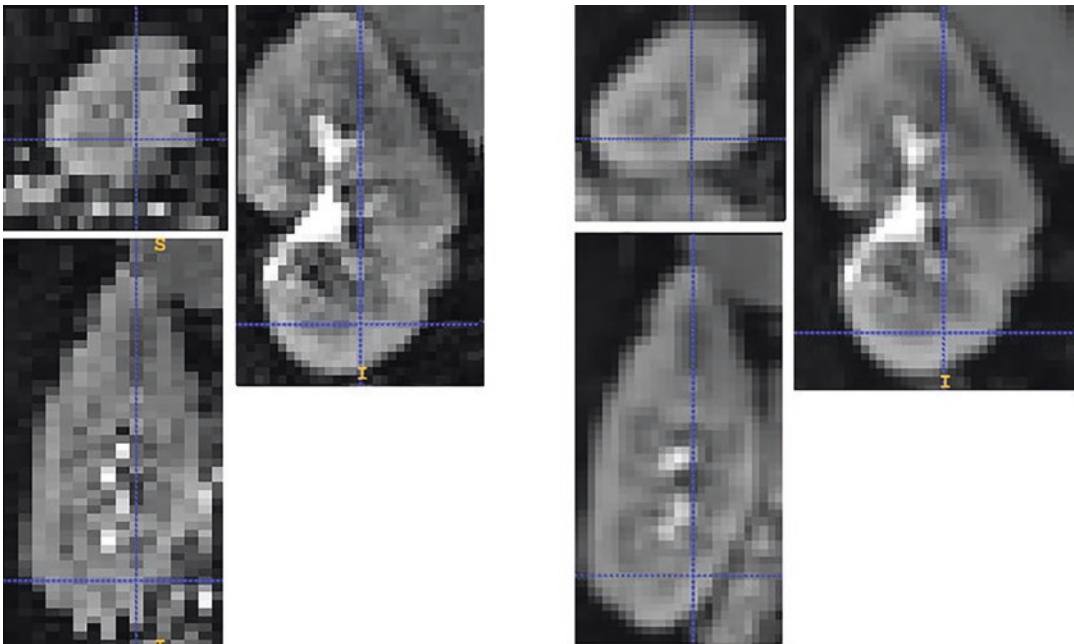


Fig. 18.8 Left panel shows an original $b = 0$ image acquired in coronal plane. The axial and sagittal views show that the slices in the original image are misaligned due to motion. Right panel shows the resultant motion-corrected $b = 0$ image. The rigid motion parameters are estimated with 3D slice to volume registration and regu-

larized based on the information content of the sequentially acquired DW-MRI slices using Kalman filtering. The resultant 3D rigid transforms are then applied to each slice and the data is reformatted to a grid. On the right panel, both axial and sagittal views show that the slices are aligned after motion correction

motion for each kidney. However, remaining non-rigid motion such as pulsatile motion may need to be corrected by a non-rigid transformation.

Motion compensation using 3D non-rigid image registration can also be used to bring the volumes acquired at different repetitions and diffusion encodings into the same physical coordinate space before fitting a signal decay model [83, 84]. However, each b -value image has different contrast; as a result, independent registration of different b -value images to a reference image (usually $b = 0$ image) can be challenging, especially for high b -value images where the signal is significantly attenuated and the signal-to-noise ratio is low. In [85], quantitative MR images are registered without using any predefined model by utilizing a PCA-based groupwise image registration technique. However, the PCA-based representation is only applicable to data from a simplified single exponential decay rather than data with an underlying complex signal decay composed of a bi-modal distribution of fast and slow diffusion components. Alternatively, signal decay model (such as IVIM) driven registration methods that perform simultaneous image registration and model estimation were proposed to account for this problem [86]. These approaches jointly solve for the image registration and quantitative parameter estimation problems. The images are registered to the corresponding volume reconstructed from the signal decay model at each b -value, which eliminates the problem of contrast differences between the moving image and the reference image during registration. Note that non-rigid registration can be challenging for acquisitions with axial slice orientation with a slice thickness of around 5–6 mm as these acquisitions have low resolution in the main direction of respiratory motion. On the other hand, acquisitions with coronal slice orientation are affected

by susceptibility artifacts leading to image distortion and moreover, distortion fields change with motion; therefore, motion and distortion correction needs to be addressed simultaneously to correct such acquisitions [55].

Common techniques for distortion correction for DW-MRI assumes that there is no motion throughout the acquisition of DW-MR images with different diffusion encodings, and therefore, the distortion field is static. The distortion field is then estimated once from a single pair of images acquired with opposite phase encoding directions and, hence, have opposite distortion effects [56, 87]. This assumption does not hold for kidney DW-MRI acquired during free-breathing due to presence of motion. Distortion field changes across images acquired at different positions of the organs. A distortion field then needs to be computed for each slice. A dual echo EPI acquisition can be used where two EPI readouts of the same slice can be acquired with opposite phase encoding directions at two echo times and used to estimate a distortion field and a distortion-corrected image for each slice [88]. This technique has been applied to DW-MRI of kidneys [55], where two EPI readouts of the same slice with left to right (L- > R) and right to left (R- > L) directions were acquired and used to estimate a distortion field for each slice. Figures 18.9 and 18.10 show how this technique was corrected for distortion in kidneys for each coronal slice. After distortion correction, the 3D slice to volume registration and motion tracking was applied to correct for the effect of motion retrospectively for all slices. Fig. 18.11 shows the effect of motion compensation and the estimated rigid motion parameters for all slices. Figure 18.12 shows IVIM and DTI parameters estimated on the original data without processing and after distortion and motion compensation (top rows) for a representative subject.

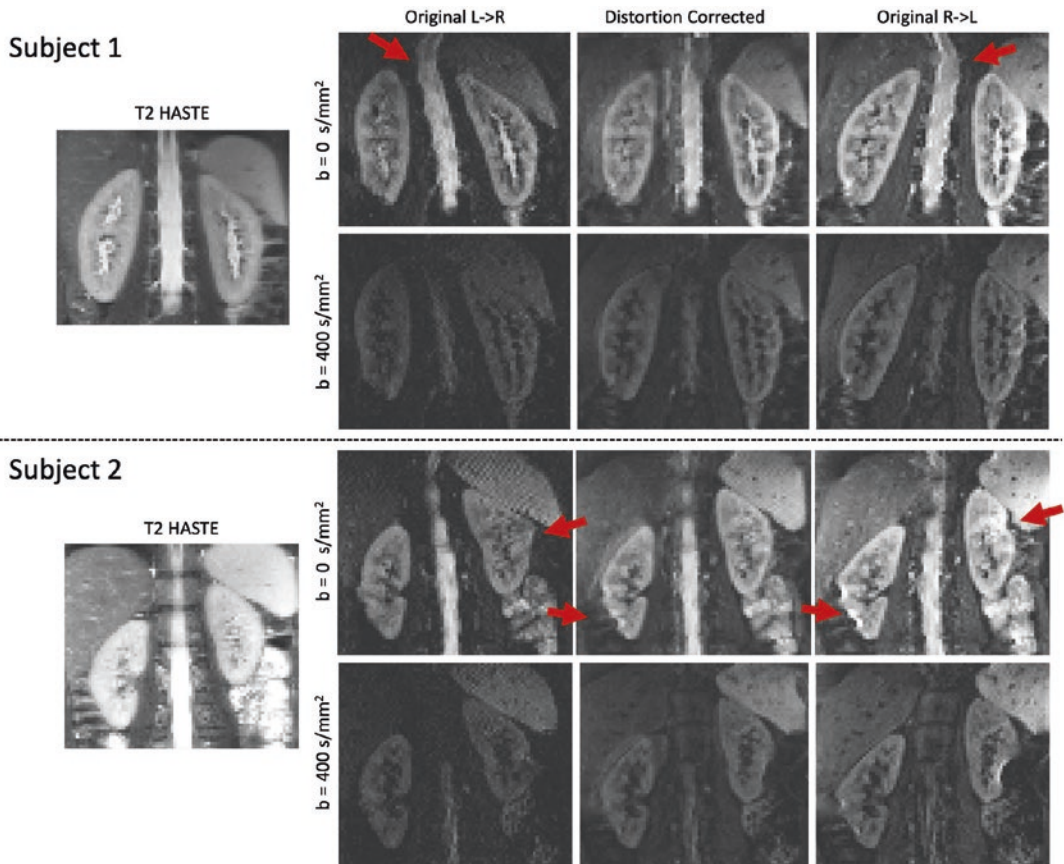


Fig. 18.9 The comparison of the reference T_2 -HASTE image of two subjects and DW-MR images (for two b -values) before and after distortion correction for two representative subjects. The T_2 -HASTE reference (left column), original L- > R image (middle left), original R- > L image (right), and distortion-corrected image (middle right) are shown. Red arrows indicate areas where

distortion is present. The original images present large distortion, particularly in the upper part of the kidneys and near the bowel, indicated with red arrows. After distortion correction, the distortion is reduced in most of the kidney, although there are some remaining errors in the right kidney of subject 2 near the bowel, also indicated by the red arrows

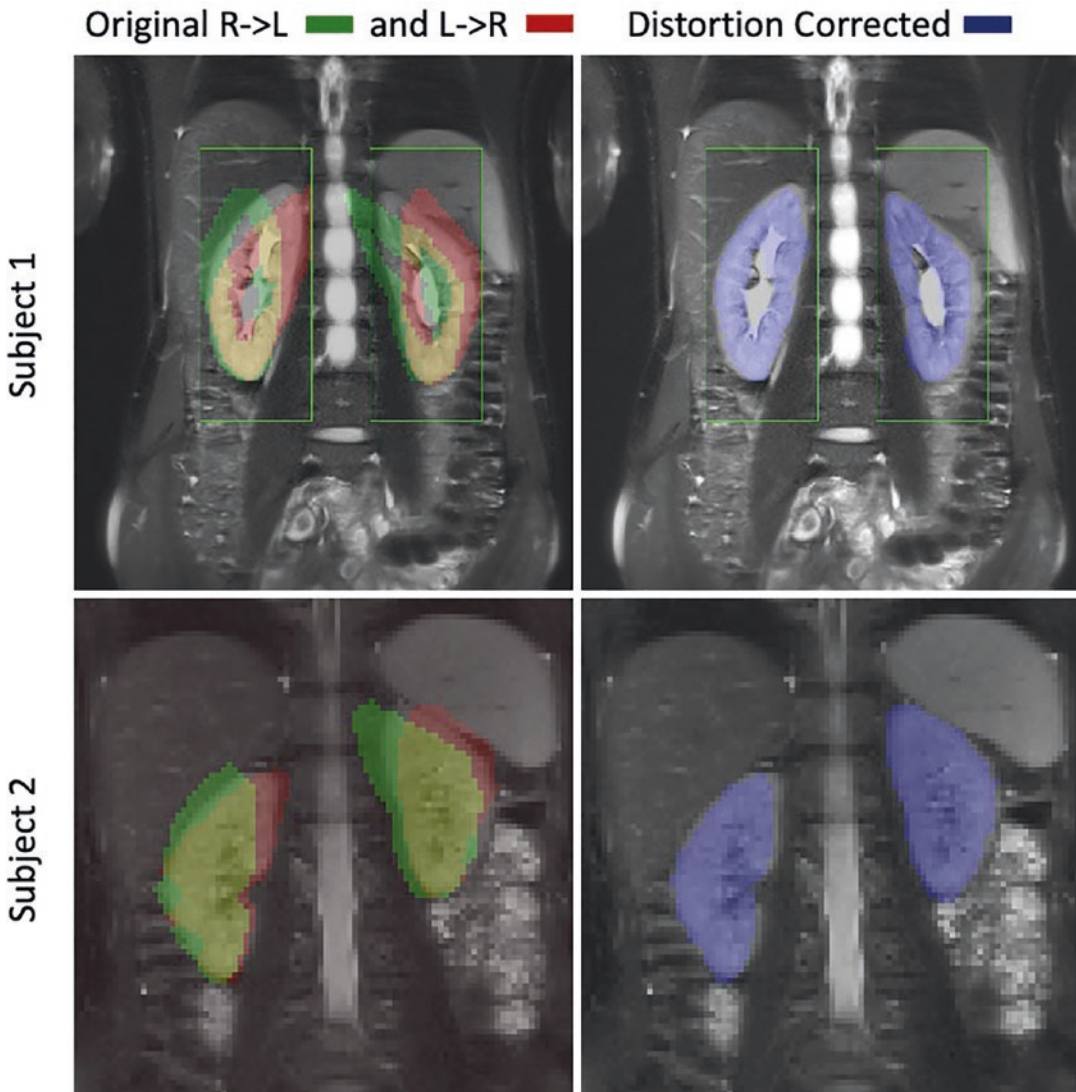


Fig. 18.10 Reference T_2 -HASTE image and the segmented kidney masks from the DW images are shown for the L- > R and R- > L images without correction on the left and for the distortion-corrected image on the right.

Each row corresponds to one representative subject. The kidneys are severely distorted in the original DW images. After distortion correction, the kidneys are in good alignment with the reference image

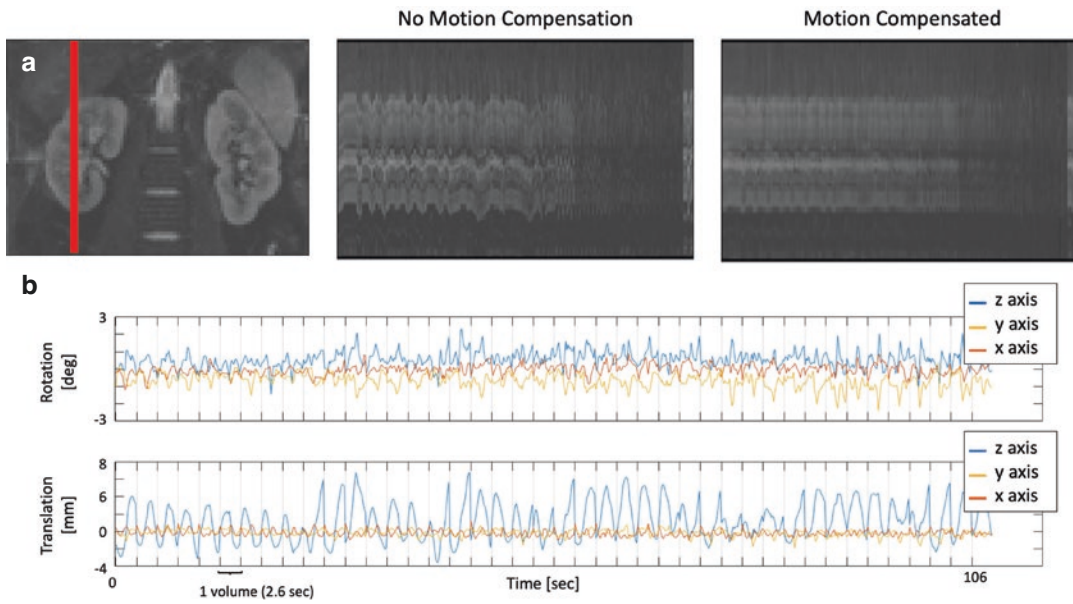


Fig. 18.11 Temporal evolution of a line of voxels from one kidney over different DW acquisitions and the registration parameters of the consecutively acquired slices during the first 1.8 min for a representative subject. The leftmost column in (a) shows the images of the cropped kidneys with a red line indicating the selected line of voxels plotted on the right. The middle panel shows the line plot for the volume with distortion correction, but no motion compensation and right panel shows the line plot

for the distortion and motion-corrected volume. Panel (b) shows the rotation and translation parameters (top and bottom). The time to acquire each volume (2.6 s) is indicated with vertical lines. Without motion compensation, the line plot shows large oscillations due to breathing. On the other hand, motion compensation corrects these oscillations and aligns the DW-MR volumes in the acquired sequence

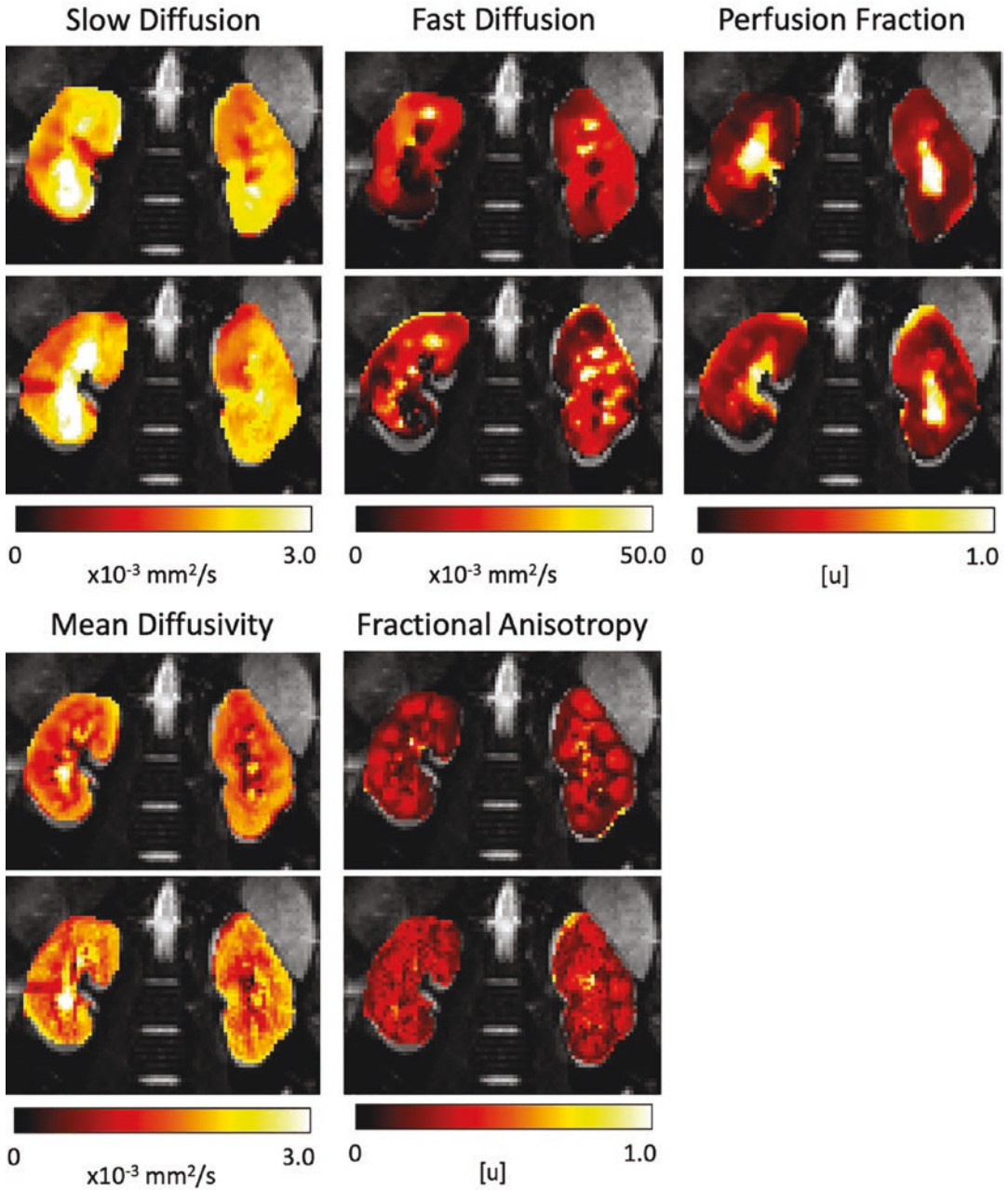


Fig. 18.12 IVIM and DTI parameters estimated on the original data without processing (no correction—bottom rows) and after distortion and motion compensation (top rows) for a representative subject. The columns correspond to the slow diffusion (D), fast diffusion (D^*), perfusion fraction (f) of the IVIM model and the mean diffusivity (MD), and fractional anisotropy (FA) param-

eters of the DTI model. The parameter maps obtained after distortion and motion compensation processing have fewer outliers and discontinuities. Moreover, the medulla and cortex can be better identified in the perfusion fraction (f) and fractional anisotropy (FA) maps of corrected images

Clinical Applications of Renal DWI

Chronic Kidney Disease

Chronic kidney disease (CKD) is a global health problem, affecting more than 10% of the world's population and more than half of adults over 70 years of age [89]. Present treatment strategies focus on slowing the progression of CKD, which requires accurate monitoring of renal function in patients with CKD. Current clinical methods of estimating renal function, such as creatine and estimated glomerular filtration rate (eGFR), have limitations as these indicators cannot reliably assess early injury and they do not reflect morphological changes in the kidneys.

There are numerous studies investigating the role of DWI in patients with CKD. A meta-analysis of DWI for staging CKD, as defined by eGFR, showed that patients with stage 1–2 CKD had lower renal ADC values than healthy subjects, and those with stage 3 CKD had higher ADC than the ones with stages 4–5 CKD [90]. There was, however, no differences in ADC values between stage 3 and stages 1–2 CKD [90]. The studies included in the analysis were hetero-

geneous with respect to b values, scanning parameters and methods for defining region of interests (ROIs), and reliable threshold levels could not be derived from the analysis. Nonetheless, this meta-analysis provides evidence for DWI in the assessment of renal function in CKD. In addition to ADC measurement, other more advanced DWI techniques have also been investigated for assessing renal function. For example, preliminary study of DTI in renal disease patients showed that fractional anisotropy (FA) was significantly lower in CKD patients than healthy controls, regardless of whether eGFR was reduced (Fig. 18.13) [91]. This may be related to the early changes in tissue microstructure and suggests the potential of DTI for early diagnosis of CKD.

A hallmark of CKD is the presence of interstitial fibrosis, which is critical for early diagnosis and treatment adaptation, and prognosis. Several clinical studies have demonstrated a good correlation between renal ADC values and histopathological fibrosis scores [73, 92–94], supporting the usefulness of DWI as a noninvasive tool for assessing renal fibrosis and monitoring CKD. Additionally, measuring the differences

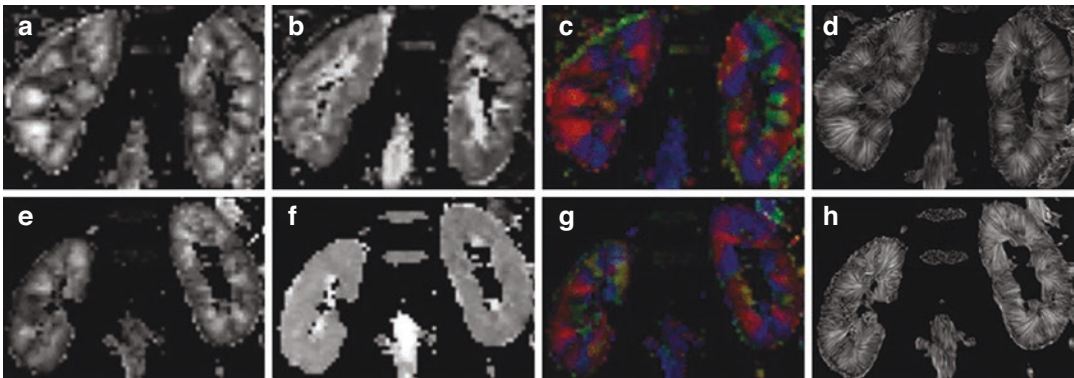


Fig. 18.13 Diffusion properties in healthy kidneys of the control group (a–d) and impaired kidneys of the study group (e–h). The coronal FA maps (a and e); A shows a higher cortico-medullary differentiation than E. The ADC maps show similar signal intensity in the cortex and

medulla (b and f). The color-coded FA maps allow the identification of the direction of diffusion (red: left-right; blue: head-foot; green: anterior-posterior) (c and g). The FA maps illustrate by texture (d and h). Figure taken with permission

between cortical and medullary ADC, termed delta-ADC, has been shown to decrease inter-individual variability and to better correlate with fibrosis in CKD [73]. In human kidneys, perfusion-induced water mobility has been reported to be much larger than the true water diffusivity [21]. Thus, IVIM imaging, which separates the true water diffusion from pseudo diffusion induced by vascular perfusion and tubular flow, has also been utilized to interrogate renal fibrosis. For example, in a study of 85 CKD patients who underwent renal biopsy, all of the IVIM parameters had a significant negative correlation with the histopathological fibrosis score [95].

The experience and promising results of DWI in kidney disease from prior studies have led to a number of ongoing multicenter clinical studies of DWI in CKD. The AFIRM (Application of Functional Renal MRI to Improve Assessment of Chronic Kidney Disease) will recruit 450 participants to investigate if multi-parametric renal MRI including DWI can characterize patients with and without CKD progression (NCT04238299). As new therapies are being developed to treat CKD, DWI is also being utilized for therapy response monitoring. The TOP-CKD (Trial of Pirfenidone to Prevent Progression in Chronic Kidney Disease) study is an ongoing clinical trial (NCT04258397) where DWI is used as a biomarker for monitoring renal fibrosis in 200 participants with CKD treated with Pirfenidone, an anti-fibrotic drug.

DWI has shown an overall outstanding potential in CKD, from early diagnosis of disease before renal functional decline to evaluation of the degree of tissue fibrosis and monitoring microstructure changes after treatment. To enable wider clinical adoption, standardizations of DWI acquisition and processing protocols, as well as large multi-center studies are necessary.

Kidney Transplant

Kidney transplantation is the most effective way to treat end stage renal disease. However, chronic

allograft injury remains one of the biggest challenges in kidney transplantation, resulting in 20–30% of the allografts failing by 10 years [96]. While several etiologies lead to chronic allograft injury, similar to native kidney diseases, the final common pathway is interstitial fibrosis and tubular atrophy. Currently, biopsy remains the standard for assessing kidney allograft pathology, either via surveillance or indication biopsies. Improved monitoring and timely diagnosis of allograft injury are needed to improve long-term allograft survival.

Several studies have demonstrated the potential of DWI to detect allograft fibrosis. In a study including 118 patients with kidney allograft who had undergone allograft biopsy, delta ADC was highly correlated with interstitial fibrosis and eGFR [97]. In a separate study of 27 patients, ADC was shown to differentiate functioning kidney allografts from fibrotic ones [98]. In addition, cortical ADC had good performance at predicting an eGFR decline of ≥ 4 mL/min/1.73 m² per year at 18 months [98]. In another study of 103 patients with renal allograft and who underwent indication biopsies, ADC was negatively correlated with interstitial fibrosis and was able to differentiate patients with versus without 50% fibrosis with an area under the curve of 0.88 [99]. Another recent study also investigated IVIM imaging in kidney transplant and found that IVIM-derived parameters allowed the stratification of patients into categories in which kidney allograft biopsy results are or are not likely to change clinical management [98]. Thus, DWI may have a role in guiding clinical management of patients with kidney transplant by selecting those most likely to benefit from allograft biopsies.

Kidney Cancer

The incidence of renal tumors has risen significantly in the last 20 years, largely due to the increased utilization of imaging with incidental discovery of many localized tumors [100]. One unmet clinical need is to noninvasively and reli-

ably distinguish benign tumors from renal cell carcinomas (RCCs) pre-operatively. Another unmet need is to noninvasively distinguish low grade indolent RCCs, which are amenable to active surveillance from high grade aggressive RCCs that require timely surgery or other definitive treatment.

DWI has been evaluated extensively in renal tumor characterization. In a meta-analysis including nine publications with 11 datasets encompassing 988 ADC measurements, DWI showed a relatively good diagnostic accuracy in differentiating malignant (RCCs and transitional cell carcinomas) from benign renal lesions (oncocytomas, angiomyolipomas, and cysts), with pooled weighted sensitivity and specificity of 88% and 72%, respectively [101]. Interestingly, the performance of ADC did not differ significantly in subgroup analysis including versus excluding renal cysts (Bosniak I-III cysts), despite the fact that cysts are known to demonstrate high ADC values. Also notably, a subgroup analysis found that studies, which excluded renal angiomyolipomas, had an obvious improvement in specificity from 63% to 84%, likely related to the observation that angiomyolipomas have restricted diffusion due to muscle and fat components [102]. IVIM has also been utilized for subtyping renal tumors. Perfusion fraction (f) and tissue diffusivity (D) derived from IVIM have been shown to differentiate among clear cell, papillary, chromophobe, and cystic RCCs, as well as benign entities like oncocytoma and angiomyolipoma [102–104]. A recent study also compared the performance of ADC and IVIM derived parameters in differentiating between malignant and benign renal tumors, and found tissue diffusivity (D) derived from IVIM is the best parameter for differentiating clear cell RCCs from benign renal tumors, and

perfusion fraction (f) is the best parameter for differentiating non-clear cell RCCs from benign renal tumors (Figs. 18.14 and 18.15) [105].

Clear cell RCCs are the most common subtype of RCCs, and noninvasive differentiation between low and high grade clear cell RCCs can help guide the selection of patients who may benefit from active surveillance versus surgery. A meta-analysis including eight DWI studies with 397 clear cell RCCs showed moderate diagnostic performance of ADC for differentiating low from high grade tumors, with pooled sensitivity and specificity of 0.78 and 0.86, respectively [105]. Substantial heterogeneity was observed among the studies included in the analysis, mainly attributed to the threshold effects with regard to the ADC cutoff value used to determine high grade tumors [105].

Similar to the case of diffuse renal disease, DWI has shown substantial promise for noninvasive characterization of localized renal tumors, which in turn will help guide clinical management to match treatment to those most likely to benefit. Standardized protocols are necessary to better establish its performance and assess impact on patient outcomes.

DTI of the kidney in children: comparison between normal kidneys and those with ureteropelvic junction (UPJ) obstruction.

In a study by Serai et Al., 118 normal kidneys from 102 patients were compared to 22 kidneys from 16 patients with UPJ obstruction [25]. Mean FA values were significantly lower (0.31 ± 0.07 ; $n = 22$) in kidneys with UPJ obstruction than normal kidneys (0.40 ± 0.08 ; $n = 118$). The study suggests that DTI derived metrics are potential biomarkers to differentiate kidneys with UPJ obstruction and assess renal parenchymal damage.

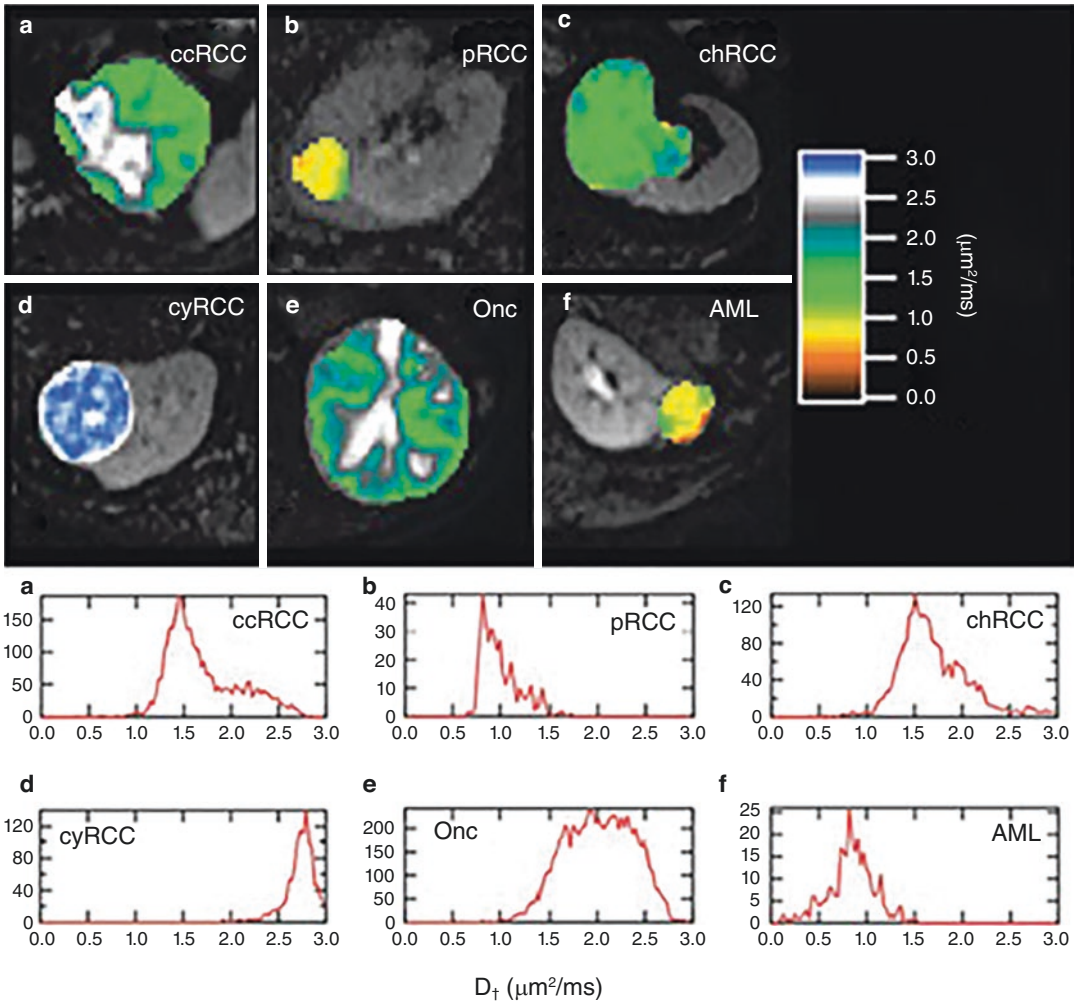


Fig. 18.14 D_t maps and corresponding voxel-wise histograms of six representative renal lesions. (a) ccRCC, (b) pRCC, (c) chRCC, (d) cyRCC, (e) Onc, and (f) AML. Although ccRCC, chRCC, and Onc have similar mean D_t values, their distribution around the means are different, reflecting varying skewness (Reproduced with permission)

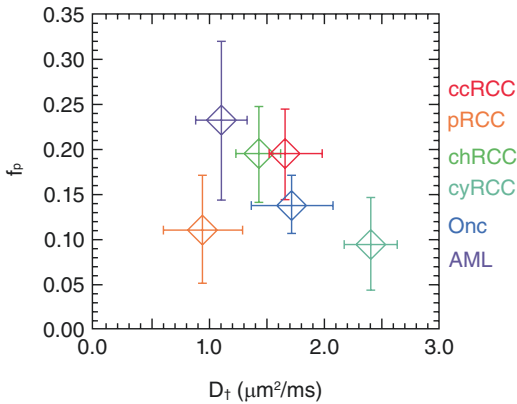


Fig. 18.15 Mean f_p values plotted against mean D_T values among six renal tumor subtypes. Data points represent mean values and error bars represent standard deviation (Reproduced with permission)

Summary

This chapter has summarized the current state of renal DWI and its most common variants, as well as highlighted the next generation of innovations in the pipeline. Recent consensus efforts by the community have also begun to migrate the growing but heterogeneous evidence base for renal DWI to the next level of translation, so that techniques and clinical data may soon be acquired sufficient to include renal DWI confidently in clinical trials of renal dysfunction (chronic kidney disease, etc.). The educational basis provided herein should help promote literacy of renal DWI within the renal community (physicists, radiologists, physiologists, and nephrologists) to further facilitate this migration.

References

1. Stejskal EO, Tanner JE. Spin diffusion measurements: spin echoes in the presence of a time-dependent field gradient. *J Chem Phys.* 1965;42(1):288–92.
2. Le Bihan D, Breton E, Lallemand D, Grenier P, Cabanis E, Laval-Jeantet M. MR imaging of intravoxel incoherent motions: application to diffusion and perfusion in neurologic disorders. *Radiology.* 1986;161(2):401–7.
3. Harada K, Fujita N, Sakurai K, Akai Y, Fujii K, Kozuka T. Diffusion imaging of the human brain:

- a new pulse sequence application for a 1.5-T standard MR system. *AJNR Am J Neuroradiol.* 1991;12(6):1143–8.
4. Sakuma H, Nomura Y, Takeda K, Tagami T, Nakagawa T, Tamagawa Y, et al. Adult and neonatal human brain: diffusional anisotropy and myelination with diffusion-weighted MR imaging. *Radiology.* 1991;180(1):229–33.
5. Bihan DL, Lima M, Federau C, Sigmund EE. Intravoxel incoherent motion (IVIM) MRI: principles and applications. 1st ed. Jenny Stanford Publishing; 2018.
6. Englund EK, Reiter DA, Shahidi B, Sigmund EE. Intravoxel incoherent motion magnetic resonance imaging in skeletal muscle: review and future directions. *J Magn Reson Imaging.* 2022;55(4):988–1012.
7. Federau C. Intravoxel incoherent motion MRI as a means to measure in vivo perfusion: a review of the evidence. *NMR Biomed.* 2017;30(11):e3780.
8. Li YT, Cercueil J-P, Yuan J, Chen W, Loffroy R, Wang YXJ. Liver intravoxel incoherent motion (IVIM) magnetic resonance imaging: a comprehensive review of published data on normal values and applications for fibrosis and tumor evaluation. *Quant Imaging Med Surg.* 2017;7(1):59–78.
9. Müller MF, Prasad PV, Edelman RR. Can the IVIM model be used for renal perfusion imaging? *Eur J Radiol.* 1998;26(3):297–303.
10. Thoeny HC, De Keyser F. Diffusion-weighted MR imaging of native and transplanted kidneys. *Radiology.* 2011;259(1):25–38.
11. Zhang JL, Sigmund EE, Chandarana H, Rusinek H, Chen Q, Vivier P-H, et al. Variability of renal apparent diffusion coefficients: limitations of the monoexponential model for diffusion quantification. *Radiology.* 2010;254(3):783–92.
12. Ljimini A, Caroli A, Laustsen C, Francis S, Mendichovszky IA, Bane O, et al. Consensus-based technical recommendations for clinical translation of renal diffusion-weighted MRI. *MAGMA.* 2020;33(1):177–95.
13. Caroli A, Schneider M, Friedli I, Ljimini A, De Seigneux S, Boor P, et al. Diffusion-weighted magnetic resonance imaging to assess diffuse renal pathology: a systematic review and statement paper. *Nephrol Dial Transplant.* 2018;33(suppl_2):ii29–40.
14. Le Bihan D, Mangin JF, Poupon C, Clark CA, Pappata S, Molko N, et al. Diffusion tensor imaging: concepts and applications. *J Magn Reson Imaging.* 2001;13(4):534–46.
15. Basser PJ, Pierpaoli C. Microstructural and physiological features of tissues elucidated by quantitative-diffusion-tensor MRI. *J Magn Reson B.* 1996;111(3):209–19.
16. Froeling M, Nederveen AJ, Nicolay K, Strijkers GJ. DTI of human skeletal muscle: the effects of diffusion encoding parameters, signal-to-noise ratio

- and T2 on tensor indices and fiber tracts. *NMR Biomed.* 2013;26(11):1339–52.
17. Jones DK. The effect of gradient sampling schemes on measures derived from diffusion tensor MRI: a Monte Carlo study. *Magn Reson Med.* 2004;51(4):807–15.
 18. Jones DK, Horsfield MA, Simmons A. Optimal strategies for measuring diffusion in anisotropic systems by magnetic resonance imaging. *Magn Reson Med.* 1999;42(3):515–25.
 19. Lanzman RS, Ljimini A, Pentang G, Zgoura P, Zenginli H, Kröpil P, et al. Kidney transplant: functional assessment with diffusion-tensor MR imaging at 3T. *Radiology.* 2013;266(1):218–25.
 20. Gaudio C, Clementi V, Busato F, Corcioni B, Orrei MG, Ferramosca E, et al. Diffusion tensor imaging and tractography of the kidneys: assessment of chronic parenchymal diseases. *Eur Radiol.* 2013;23(6):1678–85.
 21. Sigmund EE, Vivier P-H, Sui D, Lamparello NA, Tantillo K, Mikheev A, et al. Intravoxel incoherent motion and diffusion-tensor imaging in renal tissue under hydration and furosemide flow challenges. *Radiology.* 2012;263(3):758–69.
 22. Hueper K, Gutberlet M, Rodt T, Gwinner W, Lehner F, Wacker F, et al. Diffusion tensor imaging and tractography for assessment of renal allograft dysfunction-initial results. *Eur Radiol.* 2011;21(11):2427–33.
 23. Notohamiprodjo M, Glaser C, Herrmann KA, Dietrich O, Attenberger UI, Reiser MF, et al. Diffusion tensor imaging of the kidney with parallel imaging: initial clinical experience. *Investig Radiol.* 2008;43(10):677–85.
 24. Ries M, Jones RA, Basseau F, Moonen CT, Grenier N. Diffusion tensor MRI of the human kidney. *J Magn Reson Imaging.* 2001;14(1):42–9.
 25. Otero HJ, Calle-Toro JS, Maya CL, Darge K, Serai SD. DTI of the kidney in children: comparison between normal kidneys and those with ureteropelvic junction (UPJ) obstruction. *MAGMA.* 2020;33(1):63–71.
 26. Serai SD, Otero HJ, Calle-Toro JS, Berman JJ, Darge K, Hartung EA. Diffusion tensor imaging of the kidney in healthy controls and in children and young adults with autosomal recessive polycystic kidney disease. *Abdom Radiol (NY).* 2019;44(5):1867–72.
 27. Notohamiprodjo M, Chandarana H, Mikheev A, Rusinek H, Grinstead J, Feiweier T, et al. Combined intravoxel incoherent motion and diffusion tensor imaging of renal diffusion and flow anisotropy. *Magn Reson Med.* 2015;73(4):1526–32.
 28. Liu AL, Mikheev A, Rusinek H, Huang WC, Wysock JS, Babb JS, et al. Renal flow and microstructure anisotropy (REFMAP) MRI in normal and peritumoral renal tissue. *J Magn Reson Imaging.* 2018;48(1):188–97.
 29. Hilbert F, Bock M, Neubauer H, Veldhoen S, Wech T, Bley TA, et al. An intravoxel oriented flow model for diffusion-weighted imaging of the kidney. *NMR Biomed.* 2016;29(10):1403–13.
 30. Phi van V, Reiner CS, Klarhoefer M, Ciritsis A, Eberhardt C, Wurnig MC, et al. Diffusion tensor imaging of the abdominal organs: influence of oriented intravoxel flow compartments. *NMR Biomed.* 2019;32(11):e4159.
 31. Lanzman RS, Ljimini A, Müller-Lutz A, Weller J, Stabinska J, Antoch G, et al. Assessment of time-resolved renal diffusion parameters over the entire cardiac cycle. *Magn Reson Imaging.* 2019;55:1–6.
 32. Ito K, Hayashida M, Kanki A, Yamamoto A, Tamada T, Yoshida K, et al. Alterations in apparent diffusion coefficient values of the kidney during the cardiac cycle: evaluation with ECG-triggered diffusion-weighted MR imaging. *Magn Reson Imaging.* 2018;52:1–8.
 33. Wittsack H-J, Lanzman RS, Quentin M, Kuhlemann J, Klase J, Pentang G, et al. Temporally resolved electrocardiogram-triggered diffusion-weighted imaging of the human kidney: correlation between intravoxel incoherent motion parameters and renal blood flow at different time points of the cardiac cycle. *Investig Radiol.* 2012;47(4):226–30.
 34. Milani B, Ledoux J-B, Rotzinger DC, Kanemitsu M, Vallée J-P, Burnier M, et al. Image acquisition for intravoxel incoherent motion imaging of kidneys should be triggered at the instant of maximum blood velocity: evidence obtained with simulations and in vivo experiments. *Magn Reson Med.* 2019;81(1):583–93.
 35. Heusch P, Wittsack H-J, Kröpil P, Blondin D, Quentin M, Klase J, et al. Impact of blood flow on diffusion coefficients of the human kidney: a time-resolved ECG-triggered diffusion-tensor imaging (DTI) study at 3T. *J Magn Reson Imaging.* 2013;37(1):233–6.
 36. Stabinska J, Ljimini A, Frenken M, Feiweier T, Lanzman RS, Wittsack H-J. Comparison of PGSE and STEAM DTI acquisitions with varying diffusion times for probing anisotropic structures in human kidneys. *Magn Reson Med.* 2020;84(3):1518–25.
 37. van Baalen S, Leemans A, Dik P, Lilien MR, Ten Haken B, Froeling M. Intravoxel incoherent motion modeling in the kidneys: comparison of mono-, bi-, and triexponential fit. *J Magn Reson Imaging.* 2017;46(1):228–39.
 38. Periquito JS, Gladysz T, Millward JM, Delgado PR, Cantow K, Grosenick D, et al. Continuous diffusion spectrum computation for diffusion-weighted magnetic resonance imaging of the kidney tubule system. *Quant Imaging Med Surg.* 2021;11(7):3098–119.
 39. Stabinska J, Ljimini A, Zöllner HJ, Wilken E, Benkert T, Limberg J, et al. Spectral diffusion analysis of kidney intravoxel incoherent motion MRI in healthy volunteers and patients with renal pathologies. *Magn Reson Med.* 2021;85(6):3085–95.
 40. Cho GY, Kim S, Jensen JH, Storey P, Sodickson DK, Sigmund EE. A versatile flow phantom for intravoxel incoherent motion MRI. *Magn Reson Med.* 2012;67(6):1710–20.

41. Maki JH, MacFall JR, Johnson GA. The use of gradient flow compensation to separate diffusion and microcirculatory flow in MRI. *Magn Reson Med.* 1991;17(1):95–107.
42. Schneider MJ, Gaass T, Ricke J, Dinkel J, Dietrich O. Assessment of intravoxel incoherent motion MRI with an artificial capillary network: analysis of biexponential and phase-distribution models. *Magn Reson Med.* 2019;82(4):1373–84.
43. Ahlgren A, Knutsson L, Wirestam R, Nilsson M, Ståhlberg F, Topgaard D, et al. Quantification of microcirculatory parameters by joint analysis of flow-compensated and non-flow-compensated intravoxel incoherent motion (IVIM) data. *NMR Biomed.* 2016;29(5):640–9.
44. Wu D, Zhang J. The effect of microcirculatory flow on oscillating gradient diffusion MRI and diffusion encoding with dual-frequency orthogonal gradients (DEFOG). *Magn Reson Med.* 2017;77(4):1583–92.
45. Wu D, Zhang J. Evidence of the diffusion time dependence of intravoxel incoherent motion in the brain. *Magn Reson Med.* 2019;82(6):2225–35.
46. Moulin K, Aliotta E, Ennis DB. Effect of flow-encoding strength on intravoxel incoherent motion in the liver. *Magn Reson Med.* 2019;81(3):1521–33.
47. Wetscherek A, Stieltjes B, Laun FB. Flow-compensated intravoxel incoherent motion diffusion imaging. *Magn Reson Med.* 2015;74(2):410–9.
48. Kuai Z-X, Liu W-Y, Zhang Y-L, Zhu Y-M. Generalization of intravoxel incoherent motion model by introducing the notion of continuous pseudodiffusion variable. *Magn Reson Med.* 2016;76(5):1594–603.
49. Jiang L, Sun T, Liao Y, Sun Y, Qian Z, Zhang Y, et al. Probing the ballistic microcirculation in placenta using flow-compensated and non-compensated intravoxel incoherent motion imaging. *Magn Reson Med.* 2021;85(1):404–12.
50. Spinner GR, Stoeck CT, Mathez L, von Deuster C, Federau C, Kozerke S. On probing intravoxel incoherent motion in the heart-spin-echo versus stimulated-echo DWI. *Magn Reson Med.* 2019;82(3):1150–63.
51. Sigmund EE, Mikheev A, Brinkmann IM, Gilani N, Babb JS, Basukala D, et al. Cardiac phase and flow compensation effects on renal flow and microstructure anisotropy MRI in healthy human kidney. *J Magn Reson Imaging.* 2022;58(1):221–2.
52. Partridge SC, Nissan N, Rahbar H, Kitsch AE, Sigmund EE. Diffusion-weighted breast MRI: clinical applications and emerging techniques. *J Magn Reson Imaging.* 2017;45(2):337–55.
53. Mansfield P. Real-time echo-planar imaging by NMR. *Br Med Bull.* 1984;40(2):187–90.
54. Borrelli P, Cavaliere C, Basso L, Soricelli A, Salvatore M, Aiello M. Diffusion tensor imaging of the kidney: design and evaluation of a reliable processing pipeline. *Sci Rep.* 2019;9(1):12789.
55. Coll-Font J, Afacan O, Hoge S, Garg H, Shashi K, Marami B, et al. Retrospective distortion and motion correction for free-breathing DW-MRI of the kidneys using dual-Echo EPI and slice-to-volume registration. *J Magn Reson Imaging.* 2021;53(5):1432–43.
56. Lim RP, Lim JC, Teruel JR, Botterill E, Seah J-M, Farquharson S, et al. Geometric distortion correction of renal diffusion tensor imaging using the reversed gradient method. *J Comput Assist Tomogr.* 2021;45(2):218–23.
57. Hilbert F, Wech T, Neubauer H, Veldhoen S, Bley TA, Köstler H. Comparison of turbo spin Echo and Echo planar imaging for intravoxel incoherent motion and diffusion tensor imaging of the kidney at 3Tesla. *Z Med Phys.* 2017;27(3):193–201.
58. Jin N, Deng J, Zhang L, Zhang Z, Lu G, Omary RA, et al. Targeted single-shot methods for diffusion-weighted imaging in the kidneys. *J Magn Reson Imaging.* 2011;33(6):1517–25.
59. Kenkel D, Barth BK, Piccirelli M, Filli L, Finkenstädt T, Reiner CS, et al. Simultaneous multislice diffusion-weighted imaging of the kidney: a systematic analysis of image quality. *Investig Radiol.* 2017;52(3):163–9.
60. Phi Van VD, Becker AS, Ciritsis A, Reiner CS, Boss A. Intravoxel incoherent motion analysis of abdominal organs: application of simultaneous multislice acquisition. *Investig Radiol.* 2018;53(3):179–85.
61. Taron J, Weiß J, Martirosian P, Seith F, Stemmer A, Bamberg F, et al. Clinical robustness of accelerated and optimized abdominal diffusion-weighted imaging. *Investig Radiol.* 2017;52(10):590–5.
62. Tavakoli A, Krammer J, Attenberger Uil, Budjan J, Stemmer a, nickel D, et al. simultaneous multislice diffusion-weighted imaging of the kidneys at 3 T. *Investig Radiol.* 2020;55(4):233–8.
63. Xu H, Zhang N, Yang D-W, Ren A, Ren H, Zhang Q, et al. Scan time reduction in Intravoxel incoherent motion diffusion-weighted imaging and diffusion kurtosis imaging of the abdominal organs: using a simultaneous multislice technique with different acceleration factors. *J Comput Assist Tomogr.* 2021;45(4):507–15.
64. Zhang G, Sun H, Qian T, An J, Shi B, Zhou H, et al. Diffusion-weighted imaging of the kidney: comparison between simultaneous multi-slice and integrated slice-by-slice shimming echo planar sequence. *Clin Radiol.* 2019;74(4):325.e1–8.
65. Tabari A, Machado-Rivas F, Kirsch JE, Nimkin K, Gee MS. Performance of simultaneous multislice accelerated diffusion-weighted imaging for assessing focal renal lesions in pediatric patients with tuberous sclerosis complex. *Pediatr Radiol.* 2021;51(1):77–85.
66. Blaimer M, Choli M, Jakob PM, Griswold MA, Breuer FA. Multiband phase-constrained parallel MRI. *Magn Reson Med.* 2013;69(4):974–80.
67. Duan F, Zhao T, He Y, Shu N. Test-retest reliability of diffusion measures in cerebral white matter: a multiband diffusion MRI study. *J Magn Reson Imaging.* 2015;42(4):1106–16.

68. Schmitter S, Adriany G, Waks M, Moeller S, Aristova M, Vali A, et al. Bilateral multiband 4D flow MRI of the carotid arteries at 7T. *Magn Reson Med*. 2020;84(4):1947–60.
69. Chan RW, Von Deuster C, Stoeck CT, Harmer J, Punwani S, Ramachandran N, et al. High-resolution diffusion tensor imaging of the human kidneys using a free-breathing, multi-slice, targeted field of view approach. *NMR Biomed*. 2014;27(11):1300–12.
70. Schneider JT, Kalayciyan R, Haas M, Herrmann SR, Ruhm W, Hennig J, et al. Inner-volume imaging in vivo using three-dimensional parallel spatially selective excitation. *Magn Reson Med*. 2013;69(5):1367–78.
71. Xie Y, Li Y, Wen J, Li X, Zhang Z, Li J, et al. Functional evaluation of transplanted kidneys with reduced field-of-view diffusion-weighted imaging at 3T. *Korean J Radiol*. 2018;19(2):201–8.
72. Wu W, Miller KL. Image formation in diffusion MRI: a review of recent technical developments. *J Magn Reson Imaging*. 2017;46(3):646–62.
73. Friedli I, Crowe LA, de Perrot T, Berchtold L, Martin P-Y, de Seigneux S, et al. Comparison of readout-segmented and conventional single-shot for echo-planar diffusion-weighted imaging in the assessment of kidney interstitial fibrosis. *J Magn Reson Imaging*. 2017;46(6):1631–40.
74. Wu C-J, Wang Q, Zhang J, Wang X-N, Liu X-S, Zhang Y-D, et al. Readout-segmented echo-planar imaging in diffusion-weighted imaging of the kidney: comparison with single-shot echo-planar imaging in image quality. *Abdom Radiol (NY)*. 2016;41(1):100–8.
75. Notohamiprodjo M, Dietrich O, Horger W, Hornig A, Helck AD, Herrmann KA, et al. Diffusion tensor imaging (DTI) of the kidney at 3 tesla—feasibility, protocol evaluation and comparison to 1.5 tesla. *Investig Radiol*. 2010;45(5):245–54.
76. Hernando D, Zhang Y, Pirasteh A. Quantitative diffusion MRI of the abdomen and pelvis. *Med Phys*. 2022;49(4):2774–93.
77. Binser T, Thoeny HC, Eisenberger U, Stemmer A, Boesch C, Vermathen P. Comparison of physiological triggering schemes for diffusion-weighted magnetic resonance imaging in kidneys. *J Magn Reson Imaging*. 2010;31(5):1144–50.
78. Kataoka M, Kido A, Yamamoto A, Nakamoto Y, Koyama T, Isoda H, et al. Diffusion tensor imaging of kidneys with respiratory triggering: optimization of parameters to demonstrate anisotropic structures on fraction anisotropy maps. *J Magn Reson Imaging*. 2009;29(3):736–44.
79. Li Q, Wu X, Qiu L, Zhang P, Zhang M, Yan F. Diffusion-weighted MRI in the assessment of split renal function: comparison of navigator-triggered prospective acquisition correction and breath-hold acquisition. *AJR Am J Roentgenol*. 2013;200(1):113–9.
80. Liu Y, Zhong X, Czito BG, Palta M, Bashir MR, Dale BM, et al. Four-dimensional diffusion-weighted MR imaging (4D-DWI): a feasibility study. *Med Phys*. 2017 Feb;44(2):397–406.
81. Kurugol S, Marami B, Afacan O, Warfield SK, Gholipour A. Motion-robust spatially constrained parameter estimation in renal diffusion-weighted MRI by 3D motion tracking and correction of sequential slices. *Mol Imaging Reconstr Anal Mov Body Organs Stroke Imaging Treat*. 2017;10555:75–85.
82. Marami B, Scherrer B, Afacan O, Erem B, Warfield SK, Gholipour A. Motion-robust diffusion-weighted brain MRI reconstruction through slice-level registration-based motion tracking. *IEEE Trans Med Imaging*. 2016;35(10):2258–69.
83. Guyader J-M, Bernardin L, Douglas NHM, Poot DHJ, Niessen WJ, Klein S. Influence of image registration on apparent diffusion coefficient images computed from free-breathing diffusion MR images of the abdomen. *J Magn Reson Imaging*. 2015;42(2):315–30.
84. Mazaheri Y, Do RKG, Shukla-Dave A, Deasy JO, Lu Y, Akin O. Motion correction of multi-b-value diffusion-weighted imaging in the liver. *Acad Radiol*. 2012;19(12):1573–80.
85. Huizinga W, Poot DHJ, Guyader JM, Klaassen R, Coolen BF, van Kranenburg M, et al. PCA-based groupwise image registration for quantitative MRI. *Med Image Anal*. 2016;29:65–78.
86. Kurugol S, Freiman M, Afacan O, Domachevsky L, Perez-Rossello JM, Callahan MJ, et al. Motion-robust parameter estimation in abdominal diffusion-weighted MRI by simultaneous image registration and model estimation. *Med Image Anal*. 2017;39:124–32.
87. Andersson JLR, Skare S, Ashburner J. How to correct susceptibility distortions in spin-echo echo-planar images: application to diffusion tensor imaging. *NeuroImage*. 2003;20(2):870–88.
88. Afacan O, Hoge WS, Wallace TE, Gholipour A, Kurugol S, Warfield SK. Simultaneous motion and distortion correction using dual-Echo diffusion-weighted MRI. *J Neuroimaging*. 2020;30(3):276–85.
89. Levey AS, Coresh J. Chronic kidney disease. *Lancet*. 2012;379(9811):165–80.
90. Liu H, Zhou Z, Li X, Li C, Wang R, Zhang Y, et al. Diffusion-weighted imaging for staging chronic kidney disease: a meta-analysis. *Br J Radiol*. 2018;91(1091):20170952.
91. Liu Z, Xu Y, Zhang J, Zhen J, Wang R, Cai S, et al. Chronic kidney disease: pathological and functional assessment with diffusion tensor imaging at 3T MR. *Eur Radiol*. 2015;25(3):652–60.
92. Inoue T, Kozawa E, Okada H, Inukai K, Watanabe S, Kikuta T, et al. Noninvasive evaluation of kidney hypoxia and fibrosis using magnetic resonance imaging. *J Am Soc Nephrol*. 2011;22(8):1429–34.

93. Zhao J, Wang ZJ, Liu M, Zhu J, Zhang X, Zhang T, et al. Assessment of renal fibrosis in chronic kidney disease using diffusion-weighted MRI. *Clin Radiol*. 2014;69(11):1117–22.
94. Xu X, Palmer SL, Lin X, Li W, Chen K, Yan F, et al. Diffusion-weighted imaging and pathology of chronic kidney disease: initial study. *Abdom Radiol (NY)*. 2018;43(7):1749–55.
95. Mao W, Zhou J, Zeng M, Ding Y, Qu L, Chen C, et al. Intravoxel incoherent motion diffusion-weighted imaging for the assessment of renal fibrosis of chronic kidney disease: a preliminary study. *Magn Reson Imaging*. 2018;47:118–24.
96. Stegall MD, Gaston RS, Cosio FG, Matas A. Through a glass darkly: seeking clarity in preventing late kidney transplant failure. *J Am Soc Nephrol*. 2015;26(1):20–9.
97. Berchtold L, Friedli I, Crowe LA, Martinez C, Moll S, Hadaya K, et al. Validation of the corticomedullary difference in magnetic resonance imaging-derived apparent diffusion coefficient for kidney fibrosis detection: a cross-sectional study. *Nephrol Dial Transplant*. 2019;35:937.
98. Bane O, Hectors SJ, Gordic S, Kennedy P, Wagner M, Weiss A, et al. Multiparametric magnetic resonance imaging shows promising results to assess renal transplant dysfunction with fibrosis. *Kidney Int*. 2020;97(2):414–20.
99. Wang W, Yu Y, Wen J, Zhang M, Chen J, Cheng D, et al. Combination of functional magnetic resonance imaging and histopathologic analysis to evaluate interstitial fibrosis in kidney allografts. *Clin J Am Soc Nephrol*. 2019;14(9):1372–80.
100. Hollingsworth JM, Miller DC, Daignault S, Hollenbeck BK. Rising incidence of small renal masses: a need to reassess treatment effect. *J Natl Cancer Inst*. 2006;98(18):1331–4.
101. Zhang H, Gan Q, Wu Y, Liu R, Liu X, Huang Z, et al. Diagnostic performance of diffusion-weighted magnetic resonance imaging in differentiating human renal lesions (benignity or malignancy): a meta-analysis. *Abdom Radiol (NY)*. 2016;41(10):1997–2010.
102. Tanaka H, Yoshida S, Fujii Y, Ishii C, Tanaka H, Koga F, et al. Diffusion-weighted magnetic resonance imaging in the differentiation of angiomyolipoma with minimal fat from clear cell renal cell carcinoma. *Int J Urol*. 2011;18(10):727–30.
103. Chandarana H, Kang SK, Wong S, Rusinek H, Zhang JL, Arizono S, et al. Diffusion-weighted intravoxel incoherent motion imaging of renal tumors with histopathologic correlation. *Investig Radiol*. 2012;47(12):688–96.
104. Gaing B, Sigmund EE, Huang WC, Babb JS, Parikh NS, Stoffel D, et al. Subtype differentiation of renal tumors using voxel-based histogram analysis of intravoxel incoherent motion parameters. *Investig Radiol*. 2015;50(3):144–52.
105. Woo S, Suh CH, Kim SY, Cho JY, Kim SH. Diagnostic performance of DWI for differentiating high- from low-grade clear cell renal cell carcinoma: a systematic review and meta-analysis. *AJR Am J Roentgenol*. 2017;12:W1–8.